

PhysNet Meets CHARMM: A Framework for Routine Machine Learning / Molecular Mechanics Simulations

Kaisheng Song,^{†,‡,§} Silvan Käser,^{†,§} Kai Töpfer,^{†,§} Luis Itza Vazquez-Salazar,[†]
and Markus Meuwly^{*,†,¶}

[†]*Department of Chemistry, University of Basel, Klingelbergstrasse 80, CH-4056 Basel,
Switzerland.*

[‡]*School of Chemistry and Chemical Engineering, Chongqing University, Chongqing 401331,
China.*

[¶]*Department of Chemistry, Brown University, Providence, RI, USA*

[§]*These authors contributed equally*

E-mail: m.meuwly@unibas.ch

April 26, 2023

Abstract

Full dimensional potential energy surfaces (PESs) based on machine learning (ML) techniques provide means for accurate and efficient molecular simulations in the gas- and condensed-phase for various experimental observables ranging from spectroscopy to reaction dynamics. Here, the MLpot extension with PhysNet as the ML-based model for a PES is introduced into the newly developed pyCHARMM API. To illustrate conceiving, validating, refining and using a typical workflow, para-chloro-phenol is considered as an example. The main focus is on how to approach a concrete problem from a practical perspective and applications to spectroscopic observables and the free energy for the -OH torsion in solution are discussed in detail. For the computed IR spectra in the fingerprint region the computations for para-chloro-phenol in water are in good qualitative agreement with experiment carried out in CCl₄. Also, relative intensities are largely consistent with experimental findings. The barrier for rotation of the -OH group increases from ~ 3.5 kcal/mol in the gas phase to ~ 4.1 kcal/mol from simulations in water due to favourable H-bonding interactions of the -OH group with surrounding water molecules.

1 Introduction

Atomistic Simulations provide molecular-level insight into processes and properties of chemical, biological and materials systems. This includes both, simulations that follow the temporal evolution, primarily based on molecular dynamics (MD), or those that sample configurational space, i.e. Monte Carlo (MC) simulations. The underlying object for both simulation approaches is the potential energy as a function of the coordinates of all particles involved, which is the full-dimensional potential energy surface (PES). With the inter- and intra-molecular interactions described, molecular simulations can be carried out and experimentally accessible observables can be determined from sufficiently long (for MD) or

extensive (for MC) calculations. This highlights the central role PESs play for the field of atomistic simulations.

Determining sufficiently accurate, full-dimensional and eventually global PESs has remained a challenging undertaking. There are at least three aspects that make this difficult. First, modern PESs are invariably based on reference electronic structure calculations which are carried out on reference geometries. The level of quantum chemical theory that can be afforded decreases as the system size grows. In other words, for the smallest systems, e.g. He-H₂⁺,¹ full configuration interaction (FCI) calculations with large basis sets are possible whereas for small peptides, e.g. tripeptides, routine calculations for thousands of reference geometries need to resort to lower-level density functional theory (DFT) calculations with correspondingly smaller basis sets. Secondly, once the point-wise reference information has been obtained, the PES needs to be represented in one way or another as a continuous function which can be evaluated for arbitrary geometries within the reference data set. Such a representation should also provide accurate first derivatives in a computationally efficient manner. Thirdly, the representation should extrapolate reliably to regions outside those covered by the reference data, which is often the long-range part of the PES, and the resulting PES needs to be free of artifacts such as “holes”.

Over the past 15 years machine learning-based approaches have flourished in addressing the points outlined above and the field has made remarkable progress to the extent that software solutions are becoming available for routine representation and exploration of intra- and inter-molecular interactions. A non-exhaustive list are methods based on permutation-invariant polynomials (PIPs),^{2,3} neural networks (NNs) such as SchNet,⁴ PhysNet,⁵ or DeepPot-SE,⁶ kernel-based methods including (symmetrized) gradient domain machine learning ((s)GDML),^{7,8} reproducing kernel Hilbert spaces,⁹⁻¹¹ FCHL,¹² or Gaussian process regression.^{13,14} Several recent reviews aptly summarize the present state-of-the art.¹⁵⁻¹⁸

Many of the above-mentioned methods have been applied to a range of systems (gas-phase, solids) and observables (spectroscopy, reaction dynamics) and their usefulness has been demonstrated. Thus, the field is ready for user-friendly implementations of the methods together with their integration into established computer codes. The present contribution describes the use of PhysNet together with the general molecular simulation software CHARMM *via* the pyCHARMM API and the newly introduced MLPot module¹⁹ with a focus on implementation and workflow to illustrate how to conceive, in principle, a robust NN-based PES for atomistic simulations. For this, para-Cl-phenol (para-Cl-PhOH) is used as an example to highlight both, the benefits and open issues in NN-based atomistic simulations. The work is structured as follows: First, general aspects including data generation, the PhysNet architecture and its training procedure, and details concerning the ML/MM approach are outlined. Then, technical aspects regarding the PES generation, validation and refinement for para-Cl-PhOH are given before the results from the ML/MM simulations are given. Lastly, the work is summarized and discussed in a broader context.

2 Technical Aspects

2.1 Generating a Potential Energy Surface Using PhysNet

Generating a NN-based PES using a machine learning approach such as PhysNet encompasses several steps, see Figure 1. These steps include, among others: generation of reference data, selection of the hyperparameters of the architecture, fitting of the model, model evaluation and refinement.

The first step is the generation of adequate reference data. There are several strategies for this, including MD simulations using an empirical force field, *ab initio* MD,²⁰ Normal

Mode Sampling,²¹ Diffusion Monte Carlo simulations,^{22,23} Virtual reality sampling,^{24,25} or Atoms-in-Molecule Fragments (AMONS) sampling.²⁶ The initial sampling method should be selected with the final application in mind because each method presents advantages and disadvantages. For example, if chemical reactions will be studied with the final NN-based PES, generating reference information needs to be based on a representation of the energy function that allows bond-breaking and bond-formation, such as *ab initio* MD or reactive force fields.²⁷ Conventional (bi)molecular force fields would be unsuitable for this. For a broader discussion, see References 15 and 28. It should also be noted that the construction of the reference database is an iterative process, in which the model is fitted and then refined until it achieves the desired quality for the application at hand.

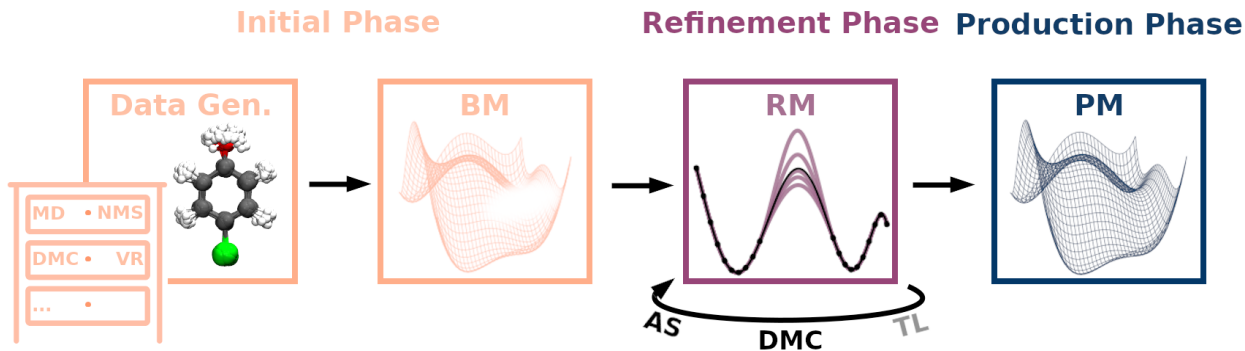


Figure 1: Schematic for the PES generation process consisting of three phases. The initial phase comprises the generation of an initial data set followed by fitting a base model. During the iterative refinement phase the data set is suitably extended to cover all (relevant) configuration space of the problem at hand and to detect and fill holes. This can for example be done using adaptive sampling and/or diffusion Monte Carlo (DMC).²³ An optional step during refinement is to improve the PES from a lower to a higher level of quantum chemical rigor, for example, using TL. The production phase includes fitting and validating the final PES used in the production simulations for computing observables. Abbreviations: **MD**: Molecular dynamics **NMS**: Normal mode sampling **DMC**: Diffusion Monte Carlo **VR**: Virtual reality **AS**: Adaptive sampling **TL**: Transfer learning **BM**: Base model **RM**: Refined model **PM**: Production model.

The next point to consider in conceiving PESs by NNs is the architecture of the model, i.e. the structure of the NN, the choice of activation functions and other technical aspects. A comprehensive description of different NN architectures can be found in Reference 28.

PhysNet, which is used in the present contribution, belongs to the family of message-passing NNs²⁹ which are a particular type of graph neural networks.³⁰ The input to PhysNet (Figure 2A) consists of the nuclear charges and the coordinates of all atoms of a molecule, which are then propagated through the different layers of the model and finally converted to the desired quantity, such as "potential energy" or "mechanical forces on atoms". The atoms' "chemical types" are encoded into an embedding vector as random values following a uniform distribution between $-\sqrt{3}$ to $\sqrt{3}$ initialized by the value of the nuclear charge. On the other hand, the coordinates of the molecule are encoded using radial basis functions (RBFs). Those radial functions aim at describing the *chemical environment* of each of the atoms in the molecule up to a predefined cutoff. The embedding vector and RBFs are then passed through N_{module} module blocks. Each of those module blocks contains an interaction layer and $N_{\text{residual}}^{\text{atomic}}$ residual layers. In the interaction layer, the embedding vector is modified by combining with the RBFs and forming a message vector. The message vector is refined by interacting with the local environment. The resulting output of the interaction layer is passed through N_{res} residual blocks. The result is then passed through the next of N_{module} module blocks and the final output layer, which converts the modified message vector to a contribution to the atomic embedding energies E_i and charges q_i . The contributions obtained from the output layer for each of the N_{module} are summed and then multiplied and shifted by learnable parameters depending on the atomic charge. Finally, the energy of the molecule of interest is obtained by summation of the embedding energies E_i of every atom predicted by the model.

$$E = \sum_{i=1}^N E_i \quad (1)$$

A known shortcoming of equation 1 is that long-range interactions are not adequately described.^{5,15} Therefore, equation 1 was extended⁵ by including the decay at long range using a function that smoothly damps the Coulombic interactions for small intermolecular distances to avoid singularities. Additional dispersion corrections to the energy, like DFT-D3,³¹ can

also be added. The final expression for the energy in PhysNet is:

$$E = \sum_{i=1}^N \left[E_i + \frac{1}{2} \sum_{j>i}^N q_i q_j \cdot \chi(r_{ij}) \right] + E_{D3} . \quad (2)$$

E_{D3} is the DFT-D3 dispersion correction and $\chi(\mathbf{r}_{ij})$ is a damping function defined as:

$$\chi(r_{ij}) = \phi(2r_{ij}) \frac{1}{\sqrt{r_{ij}^2 + 1}} + (1 - \phi(2r_{ij})) \frac{1}{r_{ij}} . \quad (3)$$

A continuous behaviour is ensured by the cutoff function $\phi(r_{ij})$.

Once the reference data is generated and the architecture for the NN model is defined; the model is fitted to the data by adjusting the weights and biases of the NN. The fitting is done by minimizing the difference between the reference values and the values predicted by NN model. The function which is minimised is the ‘‘loss function’’ and can contain different quantities. For PhysNet the loss function is

$$\begin{aligned} \mathcal{L} = & w_E |E - E^{ref}| + \frac{w_F}{3N} \sum_{i=1}^N \sum_{\alpha}^3 \left| -\frac{\partial E}{\partial r_{i,\alpha}} - F_{i,\alpha}^{ref} \right| \\ & + w_Q \left| \sum_{i=1}^N q_i - Q^{ref} \right| + \frac{w_p}{3} \sum_{\alpha=1}^3 \left| \sum_{i=1}^N q_i r_{i,\alpha} - p_{\alpha}^{ref} \right| + \mathcal{L}_{nh} . \end{aligned} \quad (4)$$

In equation 4, E^{ref} and Q^{ref} correspond to the reference energy and the total charge, $F_{i,\alpha}^{ref}$ are the Cartesian components of the force by atom, and p_{α}^{ref} are the Cartesian components of the reference dipole moment. The values of $w_i \in \{E, F, Q, p\}$ are weighting parameters that control the contribution of the different quantities to the loss function. Finally, the term \mathcal{L}_{nh} is a ‘‘nonhierarchical penalty’’ that serves as a regularization to the loss function.³² The loss function described in equation 4 is minimized by using stochastic gradient descent techniques or variations of it. Many NN-based approaches to representing molecular PESs use similar loss functions, however, other possibilities can be used as well.

The last step for constructing a NN-PES is the validation and refinement of the base model. One important method to detect “holes” in the PES is DMC sampling employing the base model.²³ Other methods³³ rely on the quantification of the uncertainty of a predicted quantity (i.e. Energy and/or Forces). Additional recommendations for validating the base model can be found in Reference 34. Independent of the method used to validate the generated potential, new samples will be added to regions that were found to be under-sampled, for example by means of adaptive sampling.³⁵ This process is repeated until the model achieves the desired accuracy. Subsequently, other techniques such as transfer learning^{36,37} (TL) or Δ -learning³⁸ can be used to enhance the quality of the potential, if only a limited number of “high” quality reference points can be obtained.

2.2 The ML/MM Approach in pyCHARMM

One particularly promising way to use machine learned PESs is in mixed machine learning/molecular mechanics (ML/MM) simulations. Such an approach follows more established mixed quantum mechanical/molecular mechanics (QM/MM) strategies in which a usually smaller part of the system is treated with a quantum chemical method whereas the larger remainder is represented as an empirical energy function.^{39–42} In ML/MM a machine learning representation, here PhysNet, is combined with an empirical force field such as CHARMM General Force Field (CGenFF) as available in the CHARMM program.^{41,43,44} This implementation into CHARMM *via* the pyCHARMM API is described next.

The pyCHARMM module is a Python library that provides functions to control the MD simulation program CHARMM via Python commands.¹⁹ It is used to combine the PhysNet PES with the functionalities of the CHARMM program such as, e.g., the classical force field algorithm, propagation methods and thermostats. PhysNet computes the potential energy and

forces for the ML-atoms together with the electrostatic interactions between the predicted fluctuating point charges of the ML-atoms and the static atomic charges of the empirically treated MM-atoms. CGenFF⁴⁴ handles the energies and forces for the remaining MM-atoms and the van-der-Waals interactions between MM- and ML-atoms. For that reason, a set of van-der-Waals parameters must be assigned to the ML-atoms.

This ML/MM approach is comparable with the mechanical embedding scheme of the QM/MM approach, where the intramolecular energy and charge distribution of the ML- or QM-atom system is not affected by the presence of the surrounding ML atoms and their partial atomic charges.^{45,46} The advantage of the current mechanical embedding scheme is the direct application of ML-based models of atomic systems trained in the gas-phase for condensed-phase simulations without additional training.

Figure 2B shows the modules which are involved in performing MD simulations in CHARMM using PhysNet. The input file to run pyCHARMM is a Python script and additional parameter and topology files are required from the user to define the atomic system, force field parameters and instructions for performing simulations based on CHARMM. The pyCHARMM module/interface evaluates and translates the commands to CHARMM-compatible instructions.¹⁹ The new MLPot module initializes an external model potential and evaluates potential energy and forces for the subset of ML-atoms together with the CHARMM force field energy. By adapting the MLPot module in the source code, it is possible to link different model potentials such as ANI²¹ or SchNet.⁴ The requirements for the model potentials are to provide potential energy and forces. If the ML-based PES does not predict atomic charges, the electrostatic contribution between assigned static point charges of the ML- and MM-atoms are computed by the empirical energy function.

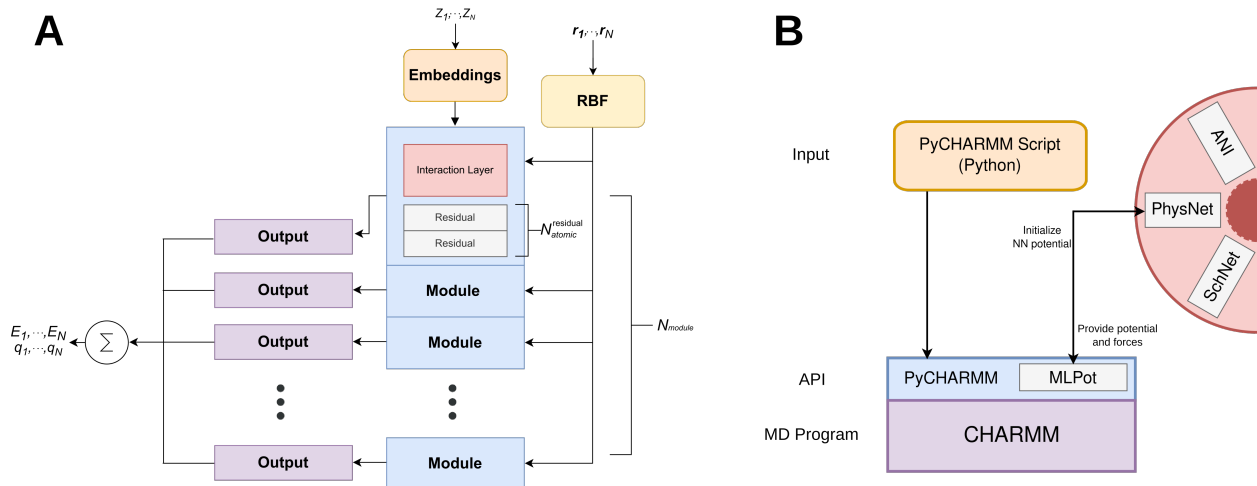


Figure 2: Panel A: Overview of the PhysNet architecture. The inputs to the model are the atomic numbers which create the 'embedding' of the different atoms and the atomic positions that are encoded through radial basis functions (RBF). Those two elements are then passed through N_{module} modules. Each module contains an interaction layer and $N_{\text{atomic}}^{\text{residual}}$ residual layers. The output of the module is passed through an output layer which returns an atomic energy and charge, which are summed to obtain the final energy and total charge of the molecule. Panel B: Schematic for initializing and integrating the PhysNet PES in simulations with the CHARMM code.

3 The PES for Para-Chloro-Phenol

This section describes the generation and testing of a full-dimensional, non-reactive PES for para-Cl-PhOH based on PhysNet. First, the data generation is described, which is followed by the training and testing of the base models (B_1 to B_N), their refinement (R_1 to R_M) and transfer learning (TL_1 to TL_K). Here, N , M , and K are independently trained models based on the same reference data set which increases in size from base to refined models whereas the data set for TL is comparatively small as the case for training from a lower level theory (MP2/6-31G(d,p)) to a higher level (MP2/aug-cc-pVTZ) is considered here.

3.1 Generation of the Reference Data

First, an initial data set needs to be generated. In the present case, this was done by running finite-temperature simulations using the semi-empirical tight binding GFN2-xTB method.⁴⁷

Simulations were run at 2000 K, 2500 K, and 3000 K, respectively and ~ 1000 reference structures per temperature were extracted at regular intervals. For all these structures, potential energies, forces and dipole moments on all atoms were determined at the MP2/6-31G(d,p) level of theory using MOLPRO2020.⁴⁸ Structures for which the single-point calculations did not converge were discarded without further analysis. All other structures were used in training 4 independent base models using energies, forces and dipole moments.

3.2 Training and Validation of the Base Model

Training of a NN-based model requires to divide the available data into “training”, “validation”, and “test” sets. For the present work, a split of 70/10/20 % (often also 80/10/10 %) was used. After initialization, the set of optimal parameters of PhysNet are determined by minimizing the loss function \mathcal{L} (Equation 4) using AMSGrad⁴⁹ and a learning rate of 10^{-3} . The batch size, which corresponds to the number of randomly chosen reference structures for which the loss is calculated at once, was set to 32. The training was terminated upon convergence (or even re-increasing due to overfitting) of the validation loss.

The performance of the best base model on energies and forces is reported in the top row of Figure 3. Here, the size of the training set was 2200 energies, corresponding forces, and dipole moments, whereas the test set contained 795 data points. Over a range of ~ 250 kcal/mol (~ 10 eV) the MAE(E) and RMSE(E) on the energies are 0.1 and 0.2 kcal/mol, respectively whereas they are 0.28 and 1.2 kcal/(mol·Å) on forces. For the test set the performance appears even better on average. It is also seen that training and test sets cover a comparable range of energies and forces. In line with the findings for the energies, the deviations in the forces (third and fourth column in Figure 3) are smaller for the test set than for the training set.

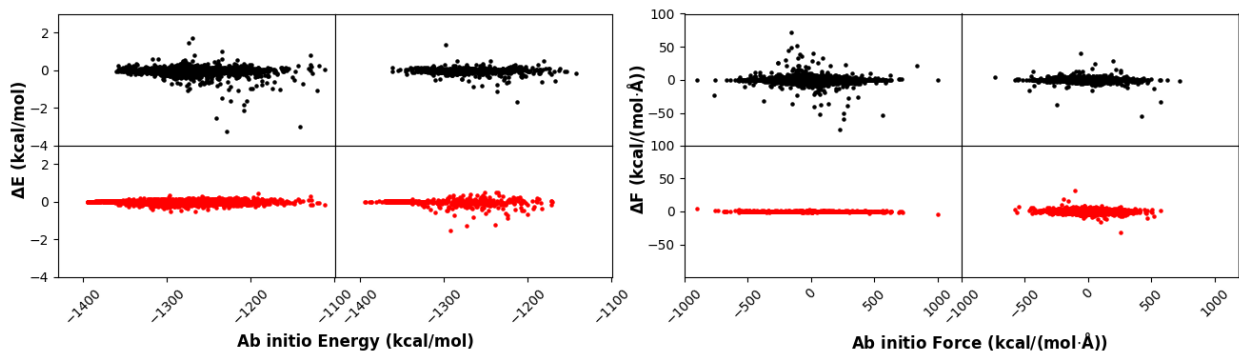


Figure 3: Comparison between reference MP2/6-31G(d,p) energies/forces and predicted energies/forces in the training and test sets, from left to right. The performance of the base and refined models for para-Cl-PhOH are shown in the upper and lower panels, respectively. Here, $\Delta E = E_{\text{PhysNet}} - E_{\text{MP2}}$, $\Delta F = F_{\text{PhysNet}}^\alpha - F_{\text{MP2}}^\alpha$ where $\alpha = (x, y, z)$ are the three Cartesian components of the forces on each atom. On the energies for the base model, the $\text{MAE}_{\text{train}}(E)$ and $\text{MAE}_{\text{test}}(E)$ are 0.11, 0.10 kcal/mol, and the corresponding $\text{RMSE}_{\text{train}}(E)$ and $\text{RMSE}_{\text{test}}(E)$ are 0.22, 0.18 kcal/mol. The $\text{MAE}_{\text{train}}(F)$ and $\text{MAE}_{\text{test}}(F)$ on forces for the base model are 0.28, 0.27 kcal/(mol·Å), and the corresponding $\text{RMSE}_{\text{train}}(F)$ and $\text{RMSE}_{\text{test}}(F)$ are 1.2, 0.89 kcal/(mol·Å). Similarly, the $\text{MAE}_{\text{train}}(E)$ and $\text{MAE}_{\text{test}}(E)$ on the energies for the refined model are 0.04, 0.07 kcal/mol, and the corresponding $\text{RMSE}_{\text{train}}(E)$ and $\text{RMSE}_{\text{test}}(E)$ are 0.06, 0.16 kcal/mol. The $\text{MAE}_{\text{train}}(F)$ and $\text{MAE}_{\text{test}}(F)$ on forces for the refined model are 0.03, 0.32 kcal/(mol·Å), and the corresponding $\text{RMSE}_{\text{train}}(F)$ and $\text{RMSE}_{\text{test}}(F)$ are 0.05, 0.80 kcal/(mol·Å).

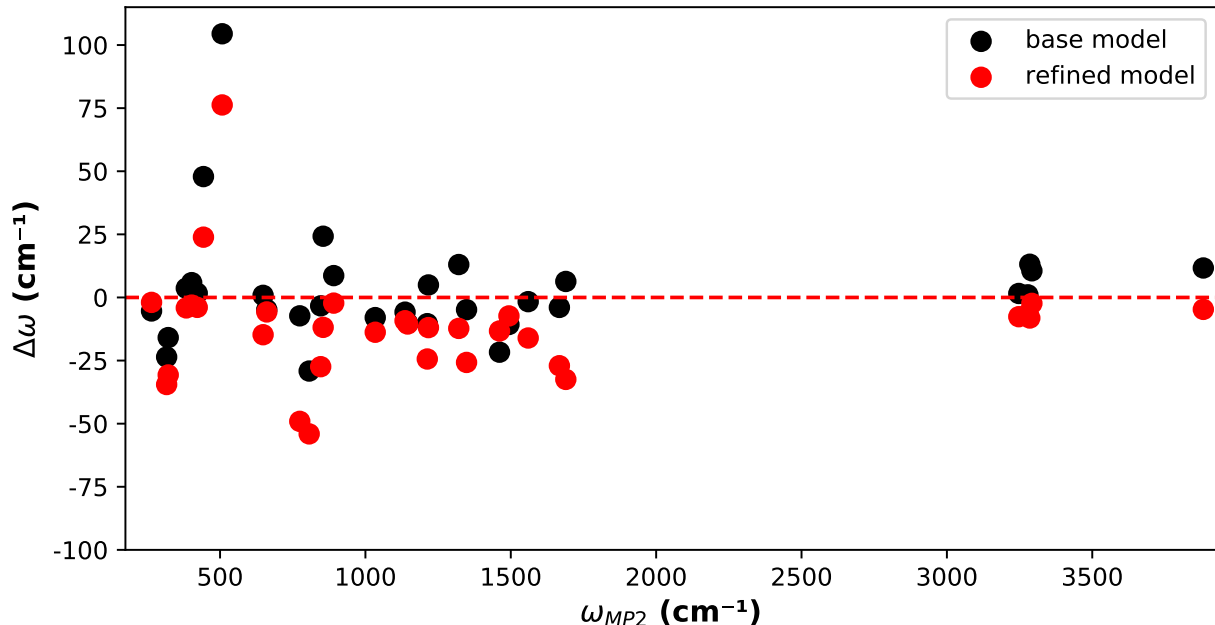


Figure 4: Accuracy of the harmonic frequencies of the base model (black dots) and refined model (red dots) with respect to the reference MP2/6-31G(d,p) values. Here, $\Delta\omega$ corresponds to $\omega_{\text{PhysNet}} - \omega_{\text{MP2}}$. For the refined model, most of the absolute deviations are obviously smaller.

As a preliminary validation of the base model, minimum energy structures and harmonic frequencies were determined from the PhysNet representation and at the MP2/6-31G(d,p) level for comparison. The root mean squared difference between the two optimized structures is 0.004 Å. This suggests that the minimum energy structure at this level of theory is reliably captured although it was not explicitly included in the training data set. Further improvements can therefore be gained by including such dedicated information either in the training set for the base model or for the refined models, see below. The difference between reference normal mode frequencies and those obtained from the base models is illustrated as black circles in Figure 4. The overall MAE and $\text{RMSE}(\omega)$ are 13 and 23 cm^{-1} , respectively, with a maximum deviation of slightly above 100 cm^{-1} . To put this into perspective, this compares to a performance of PhysNet PESs for, e.g. ten atom formic acid dimer⁵⁰ (nine atom malonaldehyde^{51,52}) with $\text{MAE}(\omega) = 2.1$ (< 5) cm^{-1} and a maximum deviation of ~ 7 (< 20) cm^{-1} . These results, however, are derived from production models that were

obtained after a refinement phase with multiple rounds of adaptive sampling. Additionally, including structures obtained from normal mode sampling²¹ or information along specific modes is likely to further improve the performance of the models.

Similarly, the base model was validated by computing the relaxed torsional potential for the OH rotation from both, the NN-model and at the MP2/6-31G(d,p) level of theory, see Figure 5. The green open circles are reference calculations at the MP2/6-31G(d,p) level whereas the black solid line is from one of the base models. Consistent with the molecular symmetry of the molecule, the two equivalent minima are isoenergetic. Except for the region around the transition state the base model closely follows the minimum energy path which was, however, not yet explicitly included in the training set. The absolute difference in the barrier height is 0.09 kcal/mol for a barrier of ~ 3.5 kcal/mol.

3.3 Refinement and Validation Using Adaptive Sampling

Usually, a single base model is not sufficient for a robust PES to be used in molecular simulations. Consequently, the model and the underlying data set need to be extended and improved by adding training samples. This can be done in various ways and the procedure opted for may also depend on the application(s) one has in mind. One established method uses adaptive sampling.³⁵ The protocol requires two or multiple independently trained base models which can employ different random seeds and/or reference data for training them. With base models B_1 to B_N finite-temperature simulations are carried out and structures are saved if the two or multiple base models differ in energy by a given threshold. In other words, the disagreement in the predictions of B_1 to B_N is used as the criterion for adding structures together with their energies and forces to the training set.

In the present case, 1000, 1500 and 1000 additional structures with an energy difference

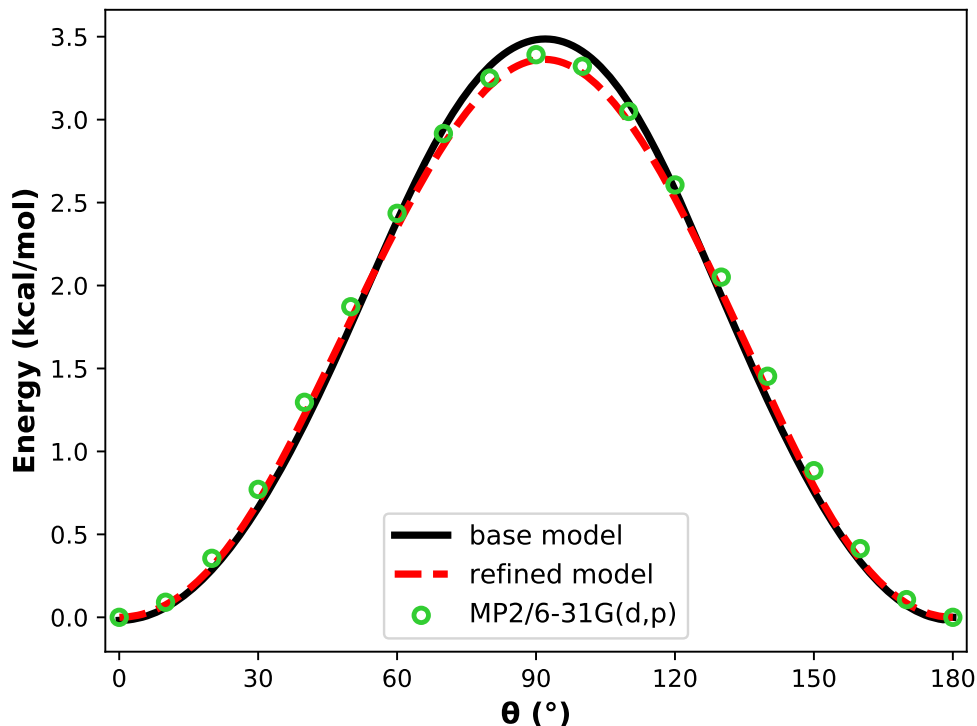


Figure 5: The energy profile of the OH torsion in para-Cl-PhOH. Here, the black solid line and red dashed line stand for the energies from the base and refined PhysNet models, respectively. The green open circles represent the reference MP2/6-31G(d,p) energies.

threshold of 0.5 kcal/mol were generated from finite-temperature simulations at 2000, 2500 and 3000 K, respectively. For these structures, MP2/6-31G(d,p) calculations were carried out and the energies and forces were added to the pool of reference data. This yielded a total of 6748 data points which were split according to 80 : 10 : 10 % into training, validation and test samples. Next, two independent models based on the refined data set were trained. The fitting errors on the training and test data are reported in the bottom row of Figure 3. Now, the errors on the training set are considerably lower than those on the test set for both, energies and forces. It is also seen that adaptive sampling adds low-energy structures which extend the energy range covered to close to 300 kcal/mol.

Validation of the refined models proceeds along the same lines as for the base model. The minimum energy structures now differ from the reference MP2/6-31G(d,p) geometries by

0.0026 Å. For the harmonic frequencies, the MAE and RMSE(ω) change to 18 and 24 cm^{-1} , respectively, i.e. both the MAE and RMSE slightly increase in comparison with the base model. Specifically, the high-frequency modes improve whereas for the low-frequency modes the average performance remains similar with the exception of the largest outlier which improves by 25 %, see Figure 4.

Finally, the OH-torsion profile was recomputed for one of the refined models. The barrier height now differs by only 0.03 kcal/mol, which is the main improvement compared with the base model. The results in Figure 5 show that adaptive sampling improves the barrier height without, however, explicitly including this information in the training set.

3.4 Transfer Learning

To further improve the quality of the PES, TL^{36,37,53} from the MP2/6-31G(d,p) to the MP2/aug-cc-pVTZ level of theory was performed. TL builds on the knowledge acquired by solving one task (representing the MP2/6-31G(d,p) PES) to solve a new, related task (representing the MP2/aug-cc-pVTZ PES).³⁶ TL and related approaches including, e.g. Δ -learning³⁸ or hierarchical ML,⁵⁴ gained a lot of attention in the field, as it allows to reach system sizes which are difficult to reach with conventional approaches.⁵⁴⁻⁵⁹ Here, the data set for TL contained 338 geometries chosen from the data set for the refined model. Besides, additional 361 geometries along the MEP of OH torsion were included to improve the performance of the model in the torsion MEP. *Ab initio* energies, forces and dipole moments for the 699 para-Cl-PhOH geometries were determined at the MP2/aug-cc-pVTZ level of theory using MOLPRO.⁴⁸ Then, the PhysNet model was retrained on the TL-data set by initializing the NN with the parameters from one of the refined models at the MP2/6-31G(d,p) level as an initial guess. The data set was split randomly according to 80/10/10 % into training/validation/test set and the learning rate was reduced to 10^{-4} compared with 10^{-3}

when learning a model from scratch.

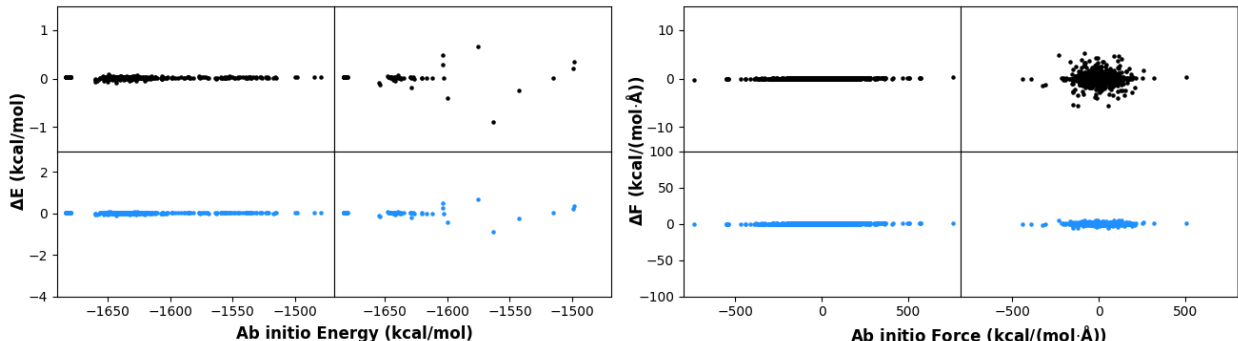


Figure 6: Comparison between reference MP2/aug-cc-pVTZ energies/forces and predicted energies/forces in the training and test sets, from left to right. The performance of the TL PhysNet model with the same scale along the y -axis as in Figure 3 is reported in the lower row and whereas the upper row has enlarged scales along the y -axis. The errors in the forces on the test set are considerably reduced compared with the base and refined models at MP2/6-31G(d,p) levels. Here, $\Delta E = E_{\text{PhysNet}} - E_{\text{MP2}}$, $\Delta F = F_{\text{PhysNet}}^\alpha - F_{\text{MP2}}^\alpha$ where $\alpha = (x, y, z)$ are the three Cartesian components of the forces on each atom. The $\text{MAE}_{\text{train}}(E)$ and $\text{MAE}_{\text{test}}(E)$ on the energies are 0.02, 0.8 kcal/mol, and the corresponding $\text{RMSE}_{\text{train}}(E)$ and $\text{RMSE}_{\text{test}}(E)$ are 0.02, 0.17 kcal/mol. On forces, the $\text{MAE}_{\text{train}}(F)$ and $\text{MAE}_{\text{test}}(F)$ are 0.01, 0.22 kcal/(mol·Å), and the corresponding $\text{RMSE}_{\text{train}}(F)$ and $\text{RMSE}_{\text{test}}(F)$ are 0.01, 0.6 kcal/(mol·Å).

The performance on the TL training and test sets for energies and forces is reported in Figure 6. The training data covers ~ 200 kcal/mol which is a somewhat narrower range than for the lower level model for which it was ~ 250 kcal/mol. For energies (columns 1 and 2 in Figure 6) the absolute error is lower than 0.1 kcal/mol throughout on the training set and never exceeds ± 1 kcal/mol on the test set. This is a considerably improved performance compared with the base models. Similarly, for forces (columns 3 and 4) the errors are much smaller than for base and refined models, see Figure 3. Importantly, TL requires only 10 % of the training effort in time compared with training base and refined models. This is seen in that the lowest value of the loss function is achieved after $\sim 10^5$ iterations whereas base and refined models were trained for $\sim 10^6$ iterations.

Testing of the transfer learned models required computation of reference data (harmonic fre-

quencies, OH torsional barriers) at the MP2/aug-cc-pVTZ level for direct comparison with predictions from PhysNet. Harmonic frequencies at the MP2/aug-cc-pVTZ level of theory for a molecule the size of para-Cl-PhOH already become prohibitive in terms of computing time and memory requirements whereas a few hundred reference calculations for energies and forces at the same level of theory can be carried out in parallel and quite efficiently. Comparison of the harmonic frequencies with their *ab initio* reference, shows that the transfer learned model predicts the values with a MAE of $\sim 16 \text{ cm}^{-1}$ and with maximum absolute deviations of less than 100 cm^{-1} . It is expected that including judiciously chosen structures in the TL data set drastically reduces the deviations for the PhysNet predictions. This has been demonstrated recently for malonaldehyde⁵² for which TL using 50 to 100 CCSD(T) quality data points were sufficient to reach $\text{MAE}(\omega) < 5 \text{ cm}^{-1}$.

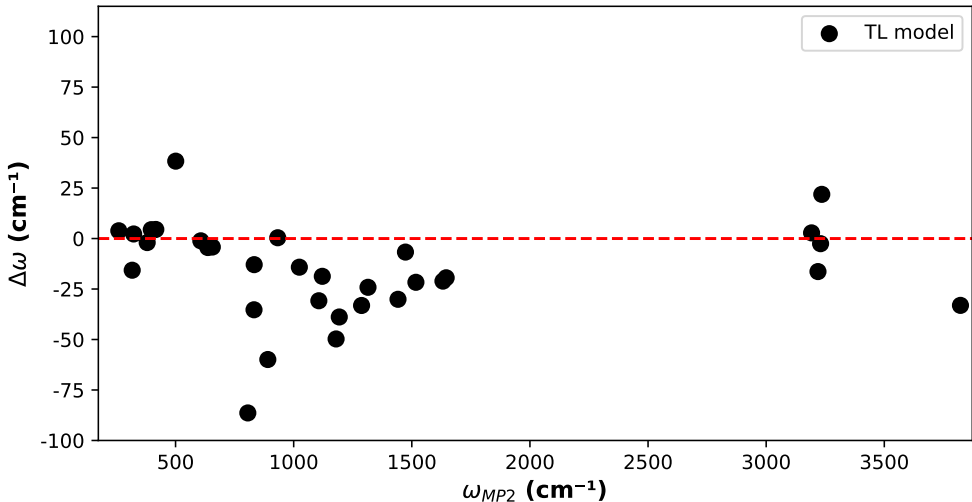


Figure 7: Transfer Learning to MP2/aug-cc-pVTZ: Comparison of the harmonic frequencies from the TL PhysNet model with the reference MP2/aug-cc-pVTZ values. Here, $\Delta\omega = \omega_{\text{PhysNet}} - \omega_{\text{MP2}}$. The average difference is 15.5 cm^{-1} . This is a comparable performance as for the base and refined models at the MP2/6-31G(d,p) level of theory.

For the OH-torsional motion the performance of the transfer learned model is excellent, see Figure 8. This training also benefits from information along the torsional MEP which was included in the data set explicitly.

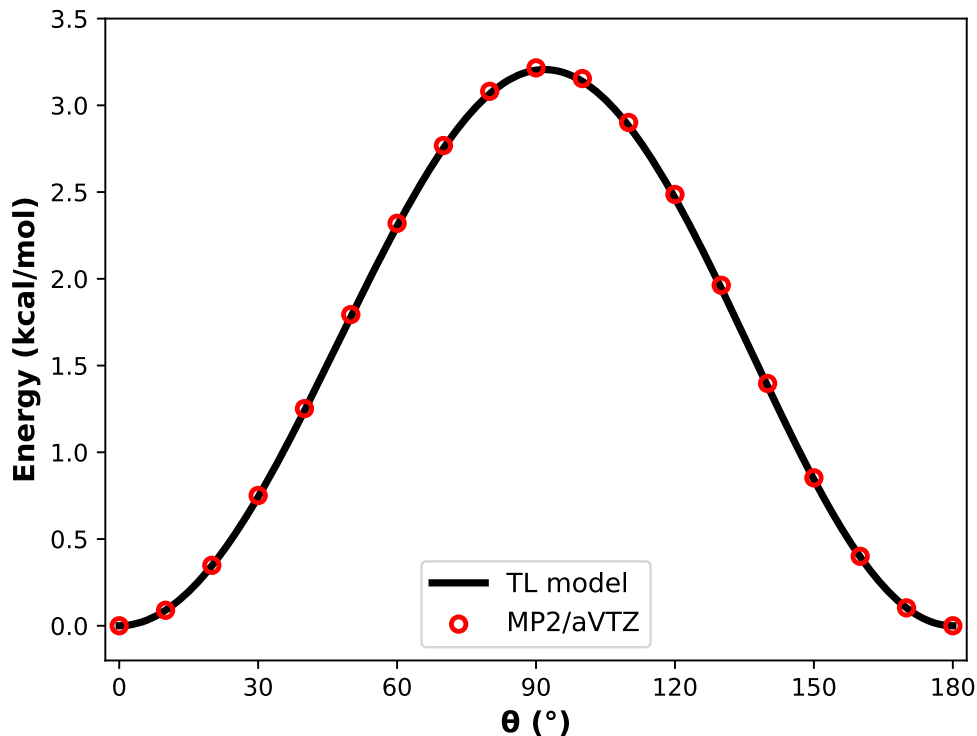


Figure 8: The energy profile of the OH torsion of the para-Cl-PhOH. Here, the black solid line represents the energies from the TL PhysNet model. The red open circles correspond to the reference energies at MP2/aug-cc-pVTZ level of theory.

4 ML/MM-MD Simulations for Para-Chloro-Phenol

Next, MD simulations for one para-Cl-PhOH molecule in a box of 881 water molecules were performed using the ML/MM approach. The intramolecular energy for para-Cl-PhOH atoms was computed by one of the trained (base, refined) PhysNet models and the TIP3P model⁶⁰ was used for water. The internal structure of each TIP3P water molecule was constrained by the SHAKE algorithm.⁶¹ The electrostatic interactions between para-Cl-PhOH and water use the fluctuating, geometry-dependent point charges for the solute together with fixed charges for the solvent. For the van-der-Waals interactions the Lorentz-Berthelot combination rules are employed together with Lennard-Jones parameters ϵ and R_{\min} from CGenFF

for the solute.⁴⁴

Initially, the structure of the solvated para-Cl-PhOH molecule in the periodic water box was relaxed by the steepest descent algorithm for 100 optimization steps. Note that initial atomic structures may be far away from the equilibrium structure and, thus, large forces act on the atoms. In such cases, the structures may get distorted to a degree which is not covered by the reference data set and reactive potentials such as PhysNet yield wrong energies and forces that even lead to chemically meaningless conformations. This affects and possibly invalidates subsequent simulations. One way to avoid this is to use empirical force fields (with fixed bond declaration) for an initial structure optimization and it is important to visually check the optimization results before launching finite-temperature MD simulations.

The partially relaxed system was heated to the target temperature of 300 K in a *NVT* simulation for a total of 50 ps with $\Delta t = 0.5$ fs. This was followed by an equilibration simulation of a *NPT* ensemble for 50 ps at 300 K and constant normal pressure with $\Delta t = 0.2$ fs. Production simulations were run in the *NPT* ensemble for 1.0 ns with $\Delta t = 0.2$ fs. To validate the correct implementation of the potential model additional constant energy simulations (*NVE*) were performed for 10 ps and $\Delta t = 0.2$ fs with initial condition from the final frame of the heating simulation. The standard deviation of the total energy in the *NVE* simulations was < 0.007 kcal/mol computed from 500 energy evaluations every 20 fs which established conservation of total energy.

Infrared (IR) spectra from the simulation data were computed from the molecular dipole moment time series $\vec{\mu}(t)$ of para-Cl-PhOH. The molecular dipole moment $\vec{\mu}(t)$ is defined by the sum of products between each atom position \vec{x}_i and its respective point charge q_i .

$$\vec{\mu}(t) = \sum_i^{N_{\text{atoms}}} \vec{x}_i \cdot q_i \tag{5}$$

The line shape of the IR spectra $I(\nu)$ as a function of the frequency ν was obtained by Fourier-transforming the dipole-dipole autocorrelation function $\langle \vec{\mu}(t) \cdot \vec{\mu}(0) \rangle$ and scaled by a quantum correction factor,⁶² $Q(\nu) = \tanh(\beta\hbar\nu/2)$.

$$I(\nu)n(\nu) \propto Q(\nu) \cdot \text{Im} \int_0^\infty dt e^{i\nu t} \sum_{i=x,y,z} \langle \mu_i(t) \cdot \mu_i(0) \rangle \quad (6)$$

This procedure yields correct lineshapes but not absolute intensities. For direct comparison, individual spectra were thus multiplied with a suitable scaling factor $n(\nu)$ to bring intensities of all spectra to comparable scales.

Figure 9 shows the computed IR spectra from MD simulation of para-Cl-PhOH in water (panel A and B) and an experimentally measured IR spectra of a 10wt% solution of para-Cl-PhOH in CCl₄. Panels A and B show the IR spectra obtained from running MD simulations using the base and refined model, respectively. In both cases, the absorption intensities of the IR spectra for frequencies above 1720 cm⁻¹ are scaled by a factor of 30 to improve the visibility of high-frequency signals in the simulated spectra.

The positions of the most intense peaks in the computed IR spectra with the PhysNet base and refined models in Figure 9A and B remain essentially unchanged. One noticeable exception is signal **c** that shows the merging of the two peaks in Panel A to a single peak in Panel B. According to the normal modes of para-Cl-PhOH signal **c** originates from the C–O stretch and C–OH bend mode. The next most intense signals **a** and **d** in the IR spectra belong to the C–Cl stretch and **a** phenol carbon lattice mode, respectively. Signal **b** can be assigned to a collective out-of-plane C–H bending mode and has no comparable, experimentally observed IR signal in Panel C (experiment in CCl₄) within its signal width. Literature reports signal **b** at a higher frequency above 800 cm⁻¹ for which a corresponding IR signal in Panel C is observed.⁶⁴ The collective four C–H and the single O–H stretch vibration correspond to signals

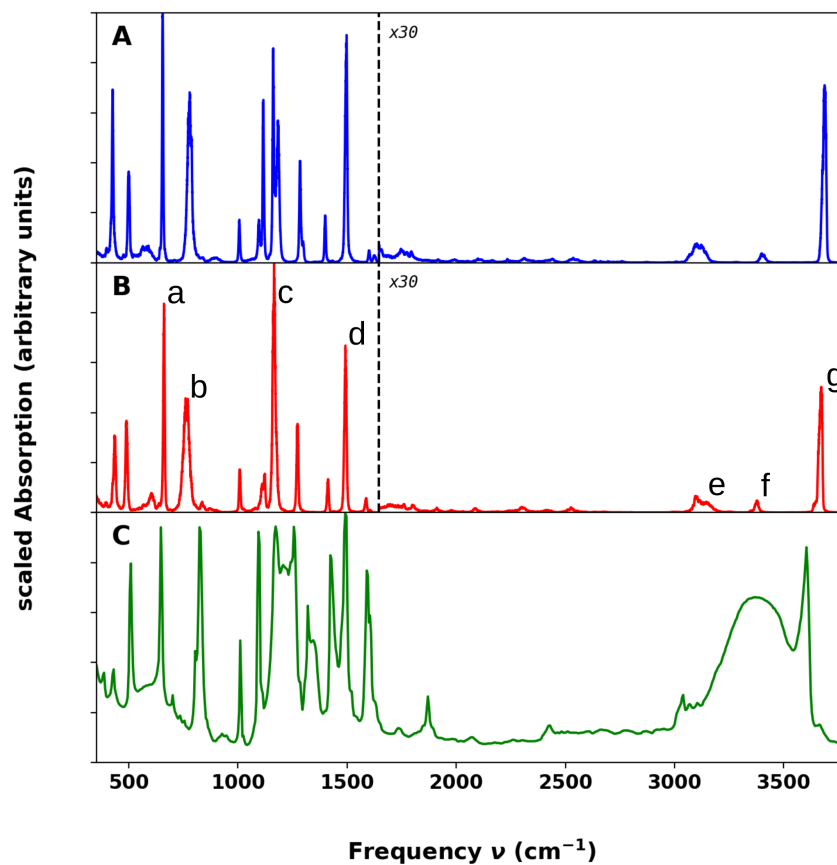


Figure 9: Simulated IR spectra from MD simulation of para-Cl-PhOH in water using the (A) PhysNet base model and (B) refined model from adaptive training. Absorption intensities for frequencies larger than 1720 cm^{-1} (marked by the vertical dashed line) are magnified by a factor of 30. Small letters a-g in Panel B are labels of selected vibrational modes. Panel C: Experimentally measured IR absorption spectra of para-Cl-PhOH (10 wt%) dissolved in CCl_4 (with contaminating water, see broad absorption below 3500 cm^{-1}).⁶³

e and **g** in Figure 9A and B, respectively, are blue-shifted compared with the experimental IR spectra in panel C. Due to anharmonicity the frequencies of signals **e** and **g** are shifted to the red compared with the harmonic frequencies of gas phase para-Cl-PhOH in Figure 4. However, the blue shift of computed line positions even from finite-temperature MD simulations compared with experiments for high-frequency (X–H) modes is a known deficiency of using classical MD simulations.⁶⁵ Even with ring polymer MD simulations the positions of these bands are shifted to higher frequencies.^{65,66} Signal **f** in the computed IR spectra in panel A and B overlaps in frequency with the broad signal in panel C around 3400 cm^{-1} , which corresponds to the stretch vibrations of water contaminating the sample. However, because water is rigid in the present simulations, the origin of feature **f** in the computed spectra remains uncertain. One possibility, supported by VPT2 calculations not discussed in detail, is the assignment of peak **f** to a combination band involving a low-frequency deformation mode of the molecule and the high frequency C–H stretching modes.

Contrary to the line positions, more significant differences are found for the relative intensities of the lines from simulations using the base and refined PESs. This difference arises because of the fluctuating charges for the two models differ. While the ratio between the intensities of the lower frequency bands are qualitatively close to the experimentally observed ones, the IR signals of the high-frequency C–H and O–H vibrations (see Figure 9 **e** and **g**, respectively) show much reduced intensities than in the experiments (note the scaling factor for the simulated IR spectra). This deficiency very likely originates from the classical dynamics approach and in particular the zero-point energy leakage.⁶⁷ In classical trajectories, it is observed that energy from vibrational modes of higher frequencies can flow to lower-frequency modes leading to smaller amplitudes of high-frequency vibrational modes and reduced intensities in the computed IR spectra line shape.

Figures 10A and B show the radial distribution function $g(r)$ between the Cl, the hydroxyl

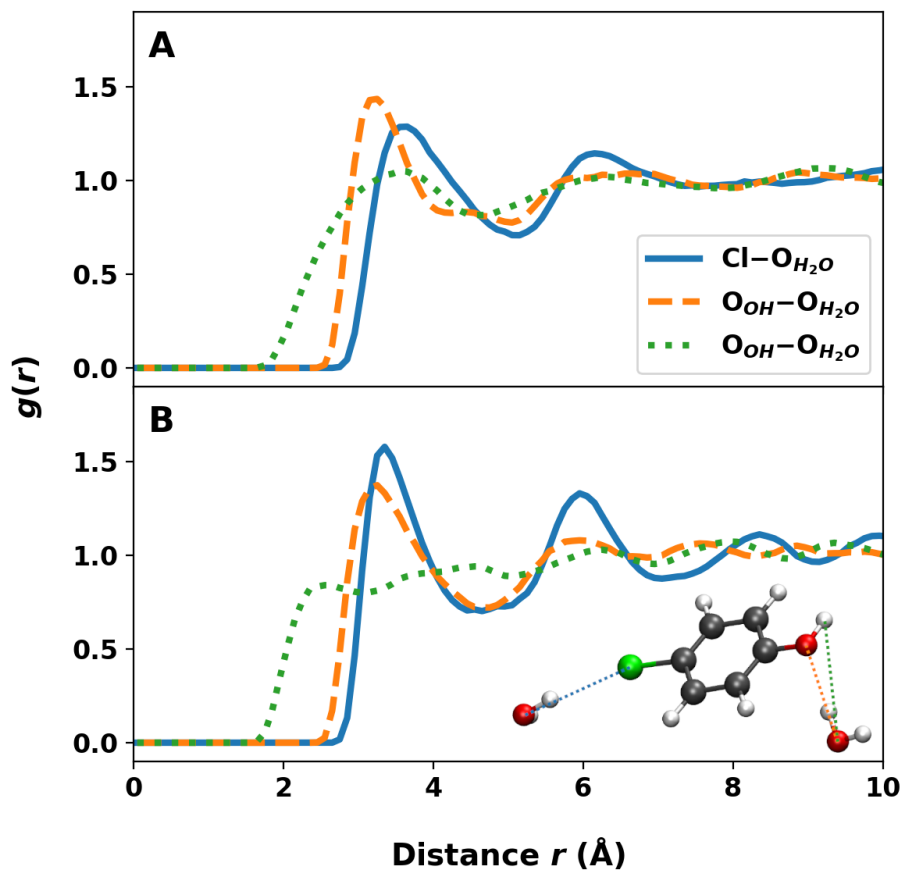


Figure 10: Radial distribution function $g(r)$ between selected atoms of para-Cl-PhOH and the oxygen atom of water solvent molecules obtained by MD simulation of para-Cl-PhOH in water using the (A) PhysNet base model and (B) refined model from adaptive sampling. The sketch in panel B visualizes the respective atom pairs by the dotted lines.

oxygen and the hydrogen atoms of para-Cl-PhOH with the oxygen atoms of water from MD simulation using the PhysNet (A) base and (B) refined model. The amplitudes of the equivalent $g(r)$ differ between the two PESs as their prediction of atomic charges differs and, as a consequence, the electrostatic interactions between para-Cl-PhOH and water changes. Such differences in the atomic charges between the base and refined PESs also cause the intensities between the computed IR spectra in Figures 9A and B to vary.

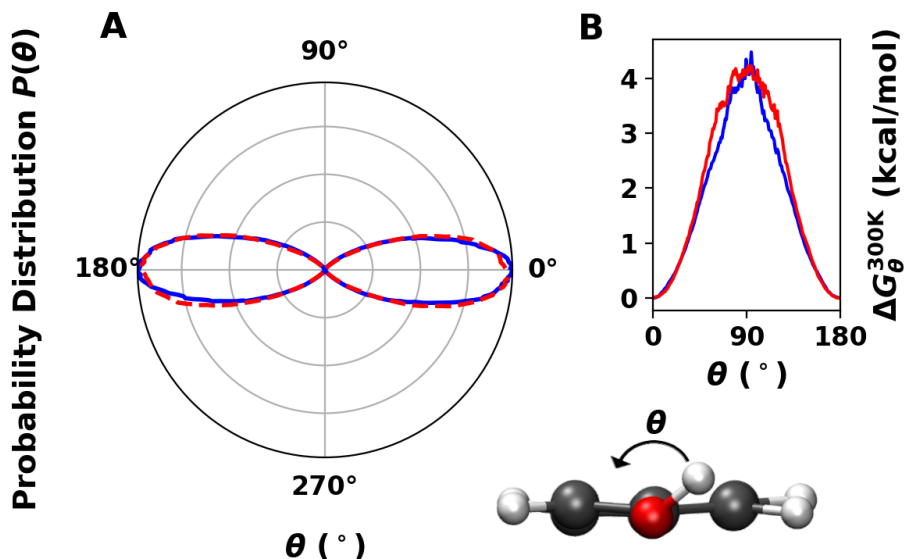


Figure 11: Polar plots of the OH torsion angle probability distribution $P(\theta)$ of para-Cl-PhOH in MD simulation using the PhysNet base model (blue) and refined model (red) from adaptive sampling. Panel B shows the free Energy profile $\Delta G(\theta)$ for rotation around the OH torsion angle derived from $P(\theta)$ according to $\Delta G(\theta) = -k_B T \ln P(\theta)$. The barrier height in water is ~ 4.1 kcal/mol compared with ~ 3.5 kcal/mol in the gas phase which amounts to an increase of $\sim 20\%$ due to the presence of solvent.

The probability distribution $P(\theta)$ for the OH torsion angle for solvated para-Cl-PhOH is shown in Figure 11A as a polar plot with maxima at 0° and 180° corresponding to planar conformations using the base (blue) and the refined PES (red dashed). The free energy profile in Figure 11B was determined from $P(\theta)$ according to $\Delta G(\theta) = -k_B T \ln P(\theta)$ for $T = 300\text{K}$. Compared with the energy profile of the OH torsion for para-Cl-PhOH in gas

phase (Figure 5), the barrier height for a 180° rotation of the OH group is ~ 4.1 kcal/mol which is ~ 0.6 kcal/mol higher than for the OH torsional barrier in the gas phase. A higher free energy barrier in solution originates from the formation of hydrogen bonds between the -OH group of para-Cl-PhOH and water molecules as the hydrogen bonds are required to break during the rotation along the OH torsion angle.

Comparing the computed IR spectra with experiments or radial distribution function from MD simulation with results derived from scattering experiments are possibilities to evaluate the accuracy of the PES and the simulation setup.^{68,69} Of particular interest is the evaluation of the intermolecular interaction potential between the ML atoms of para-Cl-PhOH and the MM atoms of water. The electrostatic contributions to the interaction potential is defined by the atomic charge prediction of the PhysNet model and the atomic charges defined by solvent model potential, respectively. The van-der-Waals potential contribution can be adapted by the modification of the Lennard-Jones parameters assigned to the ML atoms to match properties such as system density, heat capacity or solvation free energy. Although the charges on the solute respond to intramolecular geometry changes, the electrostatic potential for para-Cl-PhOH can still be further improved by using multipolar models for the electrostatics.⁷⁰⁻⁷⁴ This has, e.g., been recently done for fluoro-PhOH which only exhibits a weak sigma-hole along the C-F bond.^{75,76} For Cl-PhOH such effects will be stronger due to the pronounced sigma-hole on the chloride atom.^{75,77}

5 Summary and Outlook

In summary, the present contribution describes constructing, validating and using PhysNet PESs for spectroscopic applications. The individual steps, including reference data generation, base model fitting, refinement and TL are described, and the performance of the NN

model is illustrated at every step. The procedure described here is general and can be adapted to other applications and chemical systems. It is important to re-iterate that these are only general guidelines. For specific applications, such as photodissociation reactions,^{78–80} suitable adjustments to the steps outlined in the present work must be made. These can, for example, include the adjustment of the data generation procedure (i.e. for reactive PESs the inclusion of structures for all transition states and dissociation/isomerization/etc. pathways is required) and the simulation protocol. Irrespective of the application, PESs based on statistical methods (NNs or kernels) need to be thoroughly tested at every stage of their construction, and they need to be validated for both, generalization within the range of structures covered (interpolation) and outside that range (extrapolation).

The domain of constructing potential energy surfaces using machine learning is rapidly expanding and encompasses a wide range of data generation methods and machine learning techniques, each with its own strengths and limitations. Therefore, only a subset of these approaches have been discussed in detail in this work and broader discussions can be found in recent reviews.^{15,28,81,82} However, from a practical and software perspective it is important to stress that integration of ML-based energy functions into general molecular simulation software, as shown here for combining PhysNet with CHARMM, provides enormous "added value" to the simulation community. Although pyCHARMM has been previously used in combination with ML potentials,¹⁹ the generalization introduced here will allow the routine ML/MM simulations in CHARMM. Other benefits are that PESs for small to medium-sized molecules for spectroscopy and thermodynamic applications can include anharmonicities for all chemical bonds and the couplings between internal degrees of freedom. This has, e.g., been demonstrated previously for simulations of double proton transfer in formic acid dimer.⁴¹ "Encoding" changing bond strengths and equilibrium bond lengths depending on changes in the chemical environment within empirical energy functions is possible, but very cumbersome.⁶⁶ Hence, ML-based PESs make the full complexity of chemistry at a molecular

level visible and available in such a ML/MM//MD simulation.

For chemical reactions, which was long a domain of *ab initio* MD simulations, ML-based energy functions now provide the means to run statistically significant numbers of trajectories which was not possible before.^{79,83} More recent applications in this area include malonaldehyde in the gas phase,^{59,84} double proton transfer in hydrated formic acid dimer,⁵⁰ for atmospherically relevant reactions using permutationally invariant polynomials and NN-based energy functions,^{78,79,85} or photochemical reactions.⁸⁰ It will be interesting to see whether and how these examples, which primarily concern reactions in the gas phase, can be translated to even more complex situations such as covalent protein-ligand binding reactions for which so far primarily studies on diatomic molecules based on reproducing kernel Hilbert spaces exist.^{86–88}

Further technical developments are still possible to allow the integration of other ML potentials as ANI²¹ or SchNet⁴ following a similar strategy as the one described here. In the near future, it is desirable that the integration of these ML potentials is done directly in the main CHARMM code to improve the performance and reliability of the simulations. We plan to make further developments to the PhysNet code to allow the user to perform the steps described in an automated fashion, simplifying the setup and simulation of more complex and diverse systems.

Data Availability Statement

All scripts used for data generation, training, evaluation and use of PhysNet will be available at <https://github.com/MMunibas/physnet-pycharmm>.

References

- (1) Koner, D.; Veliz, J. C. S. V.; van der Avoird, A.; Meuwly, M. Near Dissociation States for H_2^+ -He on MRCI and FCI Potential Energy Surfaces. *Phys. Chem. Chem. Phys.* **2019**, *21*, 24976–24983.
- (2) Houston, P. L.; Qu, C.; Yu, Q.; Conte, R.; Nandi, A.; Li, J. K.; Bowman, J. M. PESPIP: Software to fit complex molecular and many-body potential energy surfaces with permutationally invariant polynomials. *J. Chem. Phys.* **2023**, *158*, 044109.
- (3) Braams, B. J.; Bowman, J. M. Permutationally Invariant Potential Energy Surfaces in High Dimensionality. *Intern. Rev. Phys. Chem.* **2009**, *28*, 577–606.
- (4) Schuett, K. T.; Saucedo, H. E.; Kindermans, P. J.; Tkatchenko, A.; Mueller, K. R. Schnet - a Deep Learning Architecture for Molecules and Materials. *J. Chem. Phys.* **2018**, *148*, 241722.
- (5) Unke, O. T.; Meuwly, M. Physnet: A Neural Network for Predicting Energies, Forces, Dipole Moments, and Partial Charges. *J. Chem. Theory Comput.* **2019**, *15*, 3678–3693.
- (6) Zhang, L.; Han, J.; Wang, H.; Saidi, W.; Car, R.; E, W. End-to-end Symmetry Preserving Inter-atomic Potential Energy Model for Finite and Extended Systems. *Advances in Neural Information Processing Systems*. 2018.
- (7) Chmiela, S.; Tkatchenko, A.; Saucedo, H. E.; Poltavsky, I.; Schütt, K. T.; Müller, K.-R. Machine learning of accurate energy-conserving molecular force fields. *Sci. Adv.* **2017**, *3*, e1603015.
- (8) Saucedo, H. E.; Chmiela, S.; Poltavsky, I.; Müller, K.-R.; Tkatchenko, A. Molecular force fields with gradient-domain machine learning: Construction and application to dynamics of small molecules with coupled cluster forces. *J. Chem. Phys.* **2019**, *150*, 114102.

- (9) Ho, T.-S.; Rabitz, H. A General Method for Constructing Multidimensional Molecular Potential Energy Surfaces from Ab Initio Calculations. *J. Chem. Phys.* **1996**, *104*, 2584–2597.
- (10) Hollebeek, T.; Ho, T.-S.; Rabitz, H. Constructing Multidimensional Molecular Potential Energy Surfaces from Ab Initio Data. *Annu. Rev. Phys. Chem.* **1999**, *50*, 537–570.
- (11) Unke, O. T.; Meuwly, M. Toolkit for the Construction of Reproducing Kernel-based Representations of Data: Application to Multidimensional Potential Energy Surfaces. *J. Chem. Inf. and Mod.* **2017**, *57*, 1923–1931.
- (12) Christensen, A. S.; Bratholm, L. A.; Faber, F. A.; Anatole von Lilienfeld, O. Fchl Revisited: Faster and More Accurate Quantum Machine Learning. *J. Chem. Phys.* **2020**, *152*, 044107.
- (13) Bartók, A. P.; Payne, M. C.; Kondor, R.; Csányi, G. Gaussian approximation potentials: The accuracy of quantum mechanics, without the electrons. *Phys. Rev. Lett.* **2010**, *104*, 136403.
- (14) Cui, J.; Krems, R. V. Efficient non-parametric fitting of potential energy surfaces for polyatomic molecules with Gaussian processes. *J. Phys. B: Atom. Mol. Opt. Phys.* **2016**, *49*, 224001.
- (15) Unke, O. T.; Chmiela, S.; Sauceda, H. E.; Gastegger, M.; Poltavsky, I.; Schütt, K. T.; Tkatchenko, A.; Müller, K.-R. Machine Learning Force Fields. *Chem. Rev.* **2021**, *121*, 10142–10186.
- (16) Manzhos, S.; Carrington Jr, T. Neural Network Potential Energy Surfaces for Small Molecules and Reactions. *Chem. Rev.* **2021**, *121*, 10187–10217.
- (17) Meuwly, M. Machine Learning for Chemical Reactions. *Chem. Rev.* **2021**, *121*, 10218–10239.

- (18) Deringer, V. L.; Bartók, A. P.; Bernstein, N.; Wilkins, D. M.; Ceriotti, M.; Csányi, G. Gaussian process regression for materials and molecules. *Chem. Rev.* **2021**, *121*, 10073–10141.
- (19) Buckner, J.; Liu, X.; Chakravorty, A.; Wu, Y.; Cervantes, L.; Lai, T.; Brooks, C. pyCHARMM: Embedding CHARMM Functionality in a Python Framework. *ChemRxiv:10.26434/chemrxiv-2023-j6wt1-v2* **2023**,
- (20) Behler, J. Four generations of high-dimensional neural network potentials. *Chem. Rev.* **2021**, *121*, 10037–10072.
- (21) Smith, J. S.; Isayev, O.; Roitberg, A. E. Ani-1: An Extensible Neural Network Potential with Dft Accuracy at Force Field Computational Cost. *Chem. Sci.* **2017**, *8*, 3192–3203.
- (22) Kosztin, I.; Faber, B.; Schulten, K. Introduction to the diffusion Monte Carlo method. *Am. J. Phys.* **1996**, *64*, 633–644.
- (23) Li, J.; Qu, C.; Bowman, J. M. Diffusion Monte Carlo with fictitious masses finds holes in potential energy surfaces. *Mol. Phys.* **2021**, *119*, e1976426.
- (24) Amabilino, S.; Bratholm, L. A.; Bennie, S. J.; Vaucher, A. C.; Reiher, M.; Glowacki, D. R. Training neural nets to learn reactive potential energy surfaces using interactive quantum chemistry in virtual reality. *J. Phys. Chem. A* **2019**, *123*, 4486–4499.
- (25) Amabilino, S.; Bratholm, L. A.; Bennie, S. J.; O’Connor, M. B.; Glowacki, D. R. Training atomic neural networks using fragment-based data generated in virtual reality. *J. Chem. Phys.* **2020**, *153*, 154105.
- (26) Huang, B.; von Lilienfeld, O. A. Quantum machine learning using atom-in-molecule-based fragments selected on the fly. *Nat. Chem.* **2020**, *12*, 945–951.

- (27) Nagy, T.; Yosa Reyes, J.; Meuwly, M. Multisurface Adiabatic Reactive Molecular Dynamics. *J. Chem. Theory Comput.* **2014**, *10*, 1366–1375.
- (28) Käser, S.; Vazquez-Salazar, L. I.; Meuwly, M.; Töpfer, K. Neural network potentials for chemistry: concepts, applications and prospects. *Dig. Discov.* **2023**, *2*, 28–58.
- (29) Gilmer, J.; Schoenholz, S. S.; Riley, P. F.; Vinyals, O.; Dahl, G. E. Neural message passing for quantum chemistry. Proc. of the 34th Int. Conf. on Machine Learning-Volume 70. 2017; pp 1263–1272.
- (30) Scarselli, F.; Gori, M.; Tsoi, A. C.; Hagenbuchner, M.; Monfardini, G. The Graph Neural Network Model. *IEEE Trans. Neural Netw.* **2009**, *20*, 61–80.
- (31) Grimme, S.; Ehrlich, S.; Goerigk, L. Effect of the damping function in dispersion corrected density functional theory. *J. Chem. Theory Comput.* **2011**, *32*, 1456–1465.
- (32) Lubbers, N.; Smith, J. S.; Barros, K. Hierarchical modeling of molecular energies using a deep neural network. *J. Chem. Phys.* **2018**, *148*, 241715.
- (33) Vazquez-Salazar, L. I.; Boittier, E. D.; Meuwly, M. Uncertainty quantification for predictions of atomistic neural networks. *Chem. Sci.* **2022**, *13*, 13068–13084.
- (34) Morrow, J. D.; Gardner, J. L.; Deringer, V. L. How to validate machine-learned interatomic potentials. *J. Chem. Phys.* **2023**, *158*, 121501.
- (35) Csányi, G.; Albaret, T.; Payne, M.; De Vita, A. “Learn on the fly”: A hybrid classical and quantum-mechanical molecular dynamics simulation. *Phys. Rev. Lett.* **2004**, *93*, 175503.
- (36) Pan, S. J.; Yang, Q. A survey on transfer learning. *IEEE Trans. Knowl. Data Eng.* **2009**, *22*, 1345–1359.
- (37) Smith, J. S.; Nebgen, B. T.; Zubatyuk, R.; Lubbers, N.; Devereux, C.; Barros, K.; Tretiak, S.; Isayev, O.; Roitberg, A. E. Approaching coupled cluster accuracy with

- a general-purpose neural network potential through transfer learning. *Nat. Commun.* **2019**, *10*, 1–8.
- (38) Ramakrishnan, R.; Dral, P.; Rupp, M.; von Lilienfeld, O. A. Big Data meets quantum chemistry approximations: The Δ -machine learning approach. *J. Chem. Theory Comput.* **2015**, *11*, 2087–2096.
- (39) Cui, Q.; Pal, T.; Xie, L. Biomolecular QM/MM simulations: What are some of the “burning issues”? *J. Phys. Chem. B* **2021**, *125*, 689–702.
- (40) Gastegger, M.; Schütt, K. T.; Müller, K.-R. Machine learning of solvent effects on molecular spectra and reactions. *Chem. Sci.* **2021**, *12*, 11473–11483.
- (41) Töpfer, K.; Käser, S.; Meuwly, M. Double proton transfer in hydrated formic acid dimer: Interplay of spatial symmetry and solvent-generated force on reactivity. *Phys. Chem. Chem. Phys.* **2022**, *24*, 13869–13882.
- (42) Lier, B.; Poliak, P.; Marquetand, P.; Westermayr, J.; Oostenbrink, C. BuRNN: Buffer Region Neural Network Approach for Polarizable-Embedding Neural Network/Molecular Mechanics Simulations. *J. Phys. Chem. Lett.* **2022**, *13*, 3812–3818.
- (43) Brooks, B. R.; Brooks III, C. L.; MacKerell Jr., A. D.; Nilsson, L.; Petrella, R. J.; Roux, B.; Won, Y.; Archontis, G.; Bartels, C.; Boresch, S. et al. Charmm: The Biomolecular Simulation Program. *J. Comput. Chem.* **2009**, *30*, 1545–1614.
- (44) Vanommeslaeghe, K.; MacKerell, A. D. Automation of the Charmm General Force Field (cgenff) I: Bond Perception and Atom Typing. *J. Chem. Inf. Model.* **2012**, *52*, 3144–3154.
- (45) Bondanza, M.; Nottoli, M.; Cupellini, L.; Lipparini, F.; Mennucci, B. Polarizable embedding QM/MM: the future gold standard for complex (bio)systems? *Phys. Chem. Chem. Phys.* **2020**, *22*, 14433–14448.

- (46) Ho, J.; Shao, Y.; Kato, J. Do better quality embedding potentials accelerate the convergence of QM/MM models? The case of solvated acid clusters. *Molecules* **2018**, *23*, 2466.
- (47) Bannwarth, C.; Ehlert, S.; Grimme, S. GFN2-xTB—An accurate and broadly parametrized self-consistent tight-binding quantum chemical method with multipole electrostatics and density-dependent dispersion contributions. *J. Chem. Theory Comput.* **2019**, *15*, 1652–1671.
- (48) Werner, H.-J.; Knowles, P. J.; Knizia, G.; Manby, F. R.; Schütz, M.; Celani, P.; Györfy, W.; Kats, D.; Korona, T.; Lindh, R. et al. MOLPRO, version 2020, a package of ab initio programs. 2020.
- (49) Reddi, S. J.; Kale, S.; Kumar, S. On the Convergence of Adam and Beyond. *arXiv e-prints* **2019**, arXiv:1904.09237.
- (50) Käser, S.; Meuwly, M. Transfer learned potential energy surfaces: accurate anharmonic vibrational dynamics and dissociation energies for the formic acid monomer and dimer. *Phys. Chem. Chem. Phys.* **2022**, *24*, 5269–5281.
- (51) Käser, S.; Unke, O. T.; Meuwly, M. Reactive Dynamics and Spectroscopy of Hydrogen Transfer from Neural Network-based Reactive Potential Energy Surfaces. *New J. Phys.* **2020**, *22*, 055002.
- (52) Käser, S.; Meuwly, M. Transfer-Learned Potential Energy Surfaces: Towards Microsecond-Scale Molecular Dynamics Simulations in the Gas Phase at CCSD(T) Quality. *arXiv e-prints* **2023**, arXiv:2303.11685.
- (53) Taylor, M. E.; Stone, P. Transfer learning for reinforcement learning domains: A survey. *J. Mach. Learn. Res.* **2009**, *10*, 1633–1685.

- (54) Dral, P. O.; Owens, A.; Dral, A.; Csányi, G. Hierarchical machine learning of potential energy surfaces. *J. Chem. Phys.* **2020**, *152*, 204110.
- (55) Nguyen, K. A.; Rossi, I.; Truhlar, D. G. A dual-level Shepard interpolation method for generating potential energy surfaces for dynamics calculations. *J. Chem. Phys.* **1995**, *103*, 5522–5530.
- (56) Nandi, A.; Qu, C.; Bowman, J. M. Using gradients in permutationally invariant polynomial potential fitting: A demonstration for CH₄ using as few as 100 configurations. *J. Chem. Theory Comput.* **2019**, *15*, 2826–2835.
- (57) Käser, S.; Boittier, E. D.; Upadhyay, M.; Meuwly, M. Transfer learning to CCSD(T): Accurate anharmonic frequencies from machine learning models. *J. Chem. Theory Comput.* **2021**, *17*, 3687–3699.
- (58) Bowman, J. M.; Qu, C.; Conte, R.; Nandi, A.; Houston, P. L.; Yu, Q. Δ -Machine Learned Potential Energy Surfaces and Force Fields. *J. Chem. Theory Comput.* **2023**, *19*, 1–17, PMID: 36527383.
- (59) Käser, S.; Richardson, J. O.; Meuwly, M. Transfer Learning for Affordable and High-Quality Tunneling Splittings from Instanton Calculations. *J. Chem. Theory Comput.* **2022**, *18*, 6840–6850.
- (60) Jorgensen, W. L.; Chandrasekhar, J.; Madura, J. D.; Impey, R. W.; Klein, M. L. Comparison of Simple Potential Functions for Simulating Liquid Water. *J. Chem. Phys.* **1983**, *79*, 926–935.
- (61) Ryckaert, J.-P.; Ciccotti, G.; Berendsen, H. J. C. Numerical Integration of the Cartesian Equations of Motion of a System with Constraints: Molecular Dynamics of N-Alkanes. *J. Chem. Phys.* **1977**, *23*, 327–341.

- (62) Ramírez, R.; López-Ciudad, T.; Kumar P, P.; Marx, D. Quantum corrections to classical time-correlation functions: Hydrogen bonding and anharmonic floppy modes. *J. Chem. Phys.* **2004**, *121*, 3973–3983.
- (63) Smith, A. *NIST Chemistry WebBook, NIST Standard Reference Database Number 69*, Eds. P.J. Linstrom and W.G. Mallard; Chapter IR Spectrum, (retrieved April 14, 2023).
- (64) Zierkiewicz, W.; Michalska, D.; Zeegers-Huyskens, T. Molecular Structures and Infrared Spectra of p-Chlorophenol and p-Bromophenol. Theoretical and Experimental Studies. *J. Phys. Chem. A* **2000**, *104*, 11685–11692.
- (65) Yu, Q.; Bowman, J. M. Classical, thermostated ring polymer, and quantum VSCF/VCI calculations of IR spectra of H_7O_3^+ and H_9O_4^+ (Eigen) and comparison with experiment. *J. Phys. Chem. A* **2019**, *123*, 1399–1409.
- (66) Xu, Z.-H.; Meuwly, M. Vibrational Spectroscopy and Proton Transfer Dynamics in Protonated Oxalate. *J. Phys. Chem. A* **2017**, *121*, 5389–5398.
- (67) Guo, Y.; Thompson, D. L.; Sewell, T. D. Analysis of the zero-point energy problem in classical trajectory simulations. *J. Chem. Phys.* **1996**, *104*, 576–582.
- (68) van Gunsteren, W. F.; Mark, A. E. Validation of molecular dynamics simulation. *J. Chem. Phys.* **1998**, *108*, 6109–6116.
- (69) van Gunsteren, W. F.; Daura, X.; Hansen, N.; Mark, A. E.; Oostenbrink, C.; Riniker, S.; Smith, L. J. Validation of Molecular Simulation: An Overview of Issues. *Angew. Chem. Int. Ed.* **2018**, *57*, 884–902.
- (70) Bereau, T.; Kramer, C.; Meuwly, M. Leveraging Symmetries of Static Atomic Multipole Electrostatics in Molecular Dynamics Simulations. *J. Chem. Theory Comput.* **2013**, *9*, 5450–5459.

- (71) Devereux, M.; Raghunathan, S.; Fedorov, D. G.; Meuwly, M. A Novel, Computationally Efficient Multipolar Model Employing Distributed Charges for Molecular Dynamics Simulations. *J. Chem. Theory Comput.* **2014**, *10*, 4229.
- (72) Unke, O. T.; Devereux, M.; Meuwly, M. Minimal Distributed Charges: Multipolar Quality at the Cost of Point Charge Electrostatics. *J. Chem. Phys.* **2017**, *147*, 161712.
- (73) Devereux, M.; Pezzella, M.; Raghunathan, S.; Meuwly, M. Polarizable Multipolar Molecular Dynamics Using Distributed Point Charges. *J. Chem. Theory Comput.* **2020**, *16*, 7267–7280.
- (74) Boittier, E. D.; Devereux, M.; Meuwly, M. Molecular Dynamics with Conformationally Dependent, Distributed Charges. *J. Chem. Theory Comput.* **2022**, *18*, 7544–7554.
- (75) Clark, T.; Hennemann, M.; Murray, J.; Politzer, P. Halogen Bonding: The σ -hole. *J. Mol. Model.* **2007**, *13*, 291–296.
- (76) Salehi, S. M.; Käser, S.; Töpfer, K.; Diamantis, P.; Pfister, R.; Hamm, P.; Rothlisberger, U.; Meuwly, M. Hydration dynamics and IR spectroscopy of 4-fluorophenol. *Phys. Chem. Chem. Phys.* **2022**, *24*, 26046–26060.
- (77) El Hage, K.; Bemish, R. J.; Meuwly, M. From in Silica to in Silico: Retention Thermodynamics at Solid-liquid Interfaces. *Phys. Chem. Chem. Phys.* **2018**, *20*, 18610–18622.
- (78) Käser, S.; Unke, O. T.; Meuwly, M. Isomerization and Decomposition Reactions of Acetaldehyde Relevant to Atmospheric Processes from Dynamics Simulations on Neural Network-based Potential Energy Surfaces. *J. Chem. Phys.* **2020**, *152*, 214304.
- (79) Upadhyay, M.; Meuwly, M. Thermal and Vibrationally Activated Decomposition of the Syn-CH₃CHOO Criegee Intermediate. *ACS Earth Space Chem.* **2021**, *5*, 3396–3406.
- (80) Westermayr, J.; Gastegger, M.; Vörös, D.; Panzenboeck, L.; Joerg, F.; González, L.;

- Marquetand, P. Deep learning study of tyrosine reveals that roaming can lead to photodamage. *Nat. Chem.* **2022**, *14*, 914–919.
- (81) Behler, J. Constructing high-dimensional neural network potentials: a tutorial review. *Int. J. Quantum Chem.* **2015**, *115*, 1032–1050.
- (82) Qu, C.; Yu, Q.; Bowman, J. M. Permutationally invariant potential energy surfaces. *Ann. Rev. Phys. Chem.* **2018**, *69*, 151–175.
- (83) Hänninen, V.; Murdachaew, G.; Nathanson, G. M.; Gerber, R. B.; Halonen, L. Ab Initio Molecular Dynamics Studies of Formic Acid Dimer Colliding with Liquid Water. *Phys. Chem. Chem. Phys.* **2018**, *20*, 23717–23725.
- (84) Schütt, K. T.; Gastegger, M.; Tkatchenko, A.; Müller, K.-R.; Maurer, R. J. Unifying machine learning and quantum chemistry with a deep neural network for molecular wavefunctions. *Nat. Comm.* **2019**, *10*, 5024.
- (85) Kidwell, N. M.; Li, H.; Wang, X.; Bowman, J. M.; Lester, M. I. Unimolecular Dissociation Dynamics of Vibrationally Activated CH₃CHOO Criegee Intermediates to OH Radical Products. *Nat. Chem.* **2016**, *8*, 509–514.
- (86) Soloviov, M.; Meuwly, M. Reproducing Kernel Potential Energy Surfaces in Biomolecular Simulations: Nitric Oxide Binding to Myoglobin. *J. Chem. Phys.* **2015**, *143*, 09B607.1.
- (87) Soloviov, M.; Das, A. K.; Meuwly, M. Structural Interpretation of Metastable States in Myoglobin-NO. *Angew. Chem. Int. Ed.* **2016**, *55*, 10126–10130.
- (88) Das, A. K.; Meuwly, M. Kinetic Analysis and Structural Interpretation of Competitive Ligand Binding for NO Dioxygenation in Truncated Hemoglobin. *Angew. Chem. Int. Ed.* **2018**, *57*, 3509–3513.